



A method to measure total atmospheric long-wave down-welling radiation using a low cost infrared thermometer tilted to the vertical



Jose L. Castro Aguilar^{a,*}, Angus R. Gentle^a, Geoff B. Smith^a, Dong Chen^b

^a Physics and Advanced Materials, University of Technology, PO Box 123, Broadway, Sydney, NSW 2007, Australia

^b CSIRO Land and Water Flagship and CSIRO Ecosystem Sciences, PO Box 56, Highett, Vic. 3190, Australia

ARTICLE INFO

Article history:

Received 27 May 2014

Received in revised form

27 October 2014

Accepted 11 December 2014

Available online 7 January 2015

Keywords:

Atmospheric long-wave down-welling radiation

Pyrgometer

Infrared thermometer

Energy efficiency

Building simulation

EnergyPlus

ABSTRACT

Atmospheric long-wave down-welling radiation is a fundamental element of climate change and of input to thermal simulation. Measuring long-wave radiation is needed to calculate locally total energy flows to the earth's surface and night cooling rates in urban precincts. It is an important parameter for the weather files used by energy building simulation software to calculate the thermal performance of buildings and their energy efficiency. Currently, atmospheric down-welling radiation is usually measured by a pyrgometer, for radiation beyond 3 μm . This is expensive and bulky. A simple methodology for measurement and calculation, with good accuracy, of average atmospheric long-wave down-welling radiation using a tilted, low-cost infrared thermometer is described. Tilt setting, comparison to data gathered by the pyrgometer, and comparison of simulation studies with both data sets is described. A link of the magnitude of divergence between instant data pairs and radiant intensity is demonstrated and shown to depend on asymmetry in cloud density.

© 2014 Elsevier Ltd. All rights reserved.

1. Introduction

There is a growing need in various research fields for nearly continuous ground level data on long-wave down-welling thermal radiation, but the scope for such data collection is limited at present by the high cost, and to some extent lack of portability, of state-of-the-art pyrgometer equipment. As a result many studies requiring such data are forced to use instead either approximate sky radiance models based on cloud cover, or data available from weather stations located many kilometres away. An approach which is: sufficiently accurate; very low cost; easy to monitor and deploy; and with a small footprint; would thus fill an important need. The method proposed here has that goal. It is based upon the link of the output of an infrared thermometer to the average thermal radiance in its field of view. A specially pre-set tilt angle is also required if the reading is to represent the mean sky radiance. The goal in many current climate and related studies is an accuracy with errors less than of 10 W m^{-2} [1] which we shall demonstrate is readily achievable for clear and uniformly overcast skies in our low cost

technique. For many partially cloudy conditions accuracy is also in or near this range.

Our own interest grew from a need for accurate down-welling thermal radiation data, primarily from the atmosphere, as input to simulation models of net thermal radiation flows from building roofs and façades, and from the surfaces around these buildings. Energy efficient building design is increasingly reliant on such simulation. Cooling rates at night are particularly sensitive to the differentials between incoming and outgoing thermal radiation flows, and these differences may dominate when local air-flow rates are small. Roofs which view much or all of the sky vault hemisphere can dominate night sky cooling, but façades can also contribute. Thermal comfort within buildings is influenced directly and indirectly by radiative cooling [2]. The storage of absorbed solar energy in façades, roofs, and exterior ground level materials such as roads and paths [3] significantly impacts on building thermal flows. Local air is heated above that of the atmosphere creating in cities an UHI (urban heat island). The four best counter measures to the UHI are to (i) minimise storage of solar heat by maximising average solar reflectance (ii) utilise evapo-transpiration in plants (iii) maximise the ability to cool exterior surfaces and interior mass at night (iv) minimize the need for air conditioning use, and maximise its efficiency when in use, to keep heat pumped to the outside low.

* Corresponding author. Tel.: +61 4 06234925; fax: +61 2 95142219.

E-mail address: jose@ecotecnics.com (J.L. Castro Aguilar).

Cooler air adjacent to a building will both improve COP (coefficient of performance) of HVAC (heating, ventilation and air conditioning) systems, and lower their use by allowing more ventilation cooling [2]. It is thus important to know as accurately as possible the variation of incoming thermal radiation intensity over time for accurate modelling of thermal performance of buildings and their surrounds. Saving more energy, improved thermal comfort, and better understanding of how to plan complete urban structures so as to limit the urban heat island problem, will follow.

Long-wave down-welling radiation is also a critical component of energy balance and global energy flows at the earth's surface [4]. Changes in average atmospheric long-wave down-welling radiation are expected as climate change evolves. The small variation year to year makes long-wave down-welling radiation at the Earth's surface an element for monitoring climate change with respect to global warming as it links on average to atmospheric temperature as well as atmospheric gas content. Radiation from local sources at night is also an important signal of an urban heat island problem but can vary widely as the field of view and position of each measurement changes. The measurement of all such flows in a novel, low cost way is the focus of this report.

A pyrgeometer is the traditional device used, and it is our reference for accuracy. It integrates the total incoming atmospheric infrared radiation with flat spectral response from $3\text{ }\mu\text{m}$ to $50\text{ }\mu\text{m}$. A coated silicon dome transmits incident radiation of wavelength longer than $3\text{ }\mu\text{m}$ and cuts off the short-wave radiation completely in the daytime [5]. Pyrgeometers also allow cloud detection and are used to separate clear-sky from cloudy-sky situations especially during dark hours [5]. Our IRT (infrared thermometer) based technique is also well suited, and easily modified for studies in urban canyons. A further advantage of the IRT's very light weight and small footprint is an ability to possibly be used on quite small UAVs (unmanned airborne vehicles) in urban situations (if allowed) to measure and map both down-welling and up-welling thermal radiation. Such very small UAVs could not cope with multiple heavy payloads. IRTs are small in area and convert IR photons which are absorbed (net of those emitted thermally) to an electrical signal using semiconductor based thermopiles. Their hot junction is in contact with a black absorber and cold junction at body temperature. IRTs have a narrower field of view to the thermopile sensor in standard pyrgeometers which also sense net absorption of IR photons, but from anywhere in the sky hemisphere. Directional sensitivity has advantages in some urban studies. However if the source of interest is the full atmosphere account must be taken of the changes in its thermal radiance with direction. This varies strongly with angle to the zenith for many wavelengths. A sensor with directional sensitivity is not ruled out but requires its tilt to be set at an angle which takes account of the specifics of the dependence of atmospheric emittance on θ the angle of tilt to the zenith, $E_A(\theta)$. Non uniform cloud cover adds axial or ϕ dependence to atmospheric emittance as $E_A(\theta, \phi)$. This impact on data from one fixed IRT is interesting, and studied to a limited extent here. It is the main error source.

Radiometric instruments which sense over a very limited field of view were first used for studying the dependence of atmospheric radiance on the zenith angle many years ago. Pioneering instruments were built by Dines in 1920 [6]. They yielded mean radiation intensities from different parts of the sky, as reported by Dines and Dines in 1927 [7]. Spherical mirrors with a limited field of view and cone half-angle of 6° , moved and collected radiation at each position from a limited portion of the sky. It was then directed onto a thermopile sensor located near the end of a 65 cm long tube. Today's pyrgeometers and most accurate infrared thermometers still use thermopile sensors. Both hence utilise the thermoelectric voltage sum generated between series of linked multiple hot and

cold junctions. The hot junction temperature is determined by the absorption of incident radiation on a black surface with which it is in good thermal contact. The junctions between different thin film, doped semiconductors at the hot and cold junctions allow modern IRTs to be compact.

A well-known improvement to Dine's device is the Link-e-Feussner system as reported by Robinson [8]. A related tubular device was used by Dalrymple and Unsworth [9], who confirmed the earlier Dines and Dines finding [7] that there is a representative angle θ_R at which detectors with very small acceptance angles can point to provide a measure of the mean sky radiance. For clear skies and completely overcast skies θ_R was found to be 52.5° to the zenith. Our IRT methodology utilises an experimentally pre-determined representative angle. We found it experimentally to be 55° . This is close to the theoretical clear sky value of 52.5° . A difference from 52.5° was expected for the IRT used due to its much larger acceptance half-angle of around 40° compared with those of the early tubular devices of around 6° . The issue of field of view sensitivity for θ_R does not appear to have been raised previously. A detailed analysis is beyond the scope of this article and will follow, but the well known rise in atmospheric emittance of the uniform sky (see section 3) as angle to the zenith rises, means θ_R is expected to vary as Ω the solid angle viewed opens up. Other impacts of $\Omega > 6^\circ$, as in IRTs, are worth briefly noting. They include reduced sensitivity of mean sky radiance results to varying tilt direction θ from $\theta_R(\Omega)$, and reduced errors relative to a full sky sensor for inhomogeneous or anisotropic cloud cover.

Another more recent highly directional pyrgeometer [1] reported by Sakai et al. aimed at further simplification of the older approaches. Their fixed tilt data was compared to that from a standard all sky, vertical pointing, Kipp and Zonnen pyrgeometer. Our overall approach uses a similar comparative methodology to evaluate the accuracy of the proposed sensor system. Our major difference from Ref. [1] is the use of a much larger field of view. Other meteorological research groups [10,11] have recently utilised an infrared temperature sensor, for example to establish the water vapour content in the atmosphere.

Our ultimate goal is accurate thermal simulation [12]. Model accuracy requires that explicit account of actual incoming thermal radiation is required. This also means that net radiation loss cannot be treated as part of an approximate combined heat transfer coefficient (with convection). It also means as we have found explicitly that approximate sky models in common use are inaccurate for roof cooling studies at night [13]. Among many simulation models available for studying thermal flows in buildings some have oversimplified the theoretical treatment of radiative flows. In the following results a comparison of models and data on a roof will be used to highlight the need for both accurate down-welling thermal radiation data, and for algorithms which treat radiative fluxes explicitly and correctly. The accuracy of this approach to simulation when IRT data is used to establish atmospheric radiance, is demonstrated in section 5 by modelling also with simultaneous pyrgeometric data.

2. The pyrgeometer and infrared thermometer

Fig. 1 shows the pyrgeometer MS-202 from Eko Instruments [14] used to gather accurate atmospheric infrared radiation. This sensor utilises a silicon dome which transmits radiation of wavelength longer than $3\text{ }\mu\text{m}$ and cuts off any incident solar radiation. The sensor has response time of about 3 s and voltage output is linear in the incident radiation to within $\pm 1\%$. A separate measure is taken of the body temperature T_B using the most accurate measure available, a four-wire Pt100 probe with accuracy to $\pm 0.15^\circ\text{C}$. The outputs of sky temperature in an IRT and down-welling radiant intensity in



Fig. 1. Pyradiometer MS-202 from Eko instruments [14].

a standard pyrgeometer are determined by a similar overall process. Both use thermopile voltage output and measurement of body temperature, hence two distinct readings. The first is a measure of heat gained from *net* thermal radiation in-flow. This comes from the amount of input radiance IR_{DW} which is absorbed, less that radiated out (IR_{OUT}). The thermal sensor voltage reading in mV depends thus on the absorbed thermal radiation which generates heat $Q_{IR,S} = [A_{IR,S} \cdot (IR_{DW} - IR_{OUT})]$, with sensor $A_{IR,S}$ the sensor's IR absorptance. Its thermal emittance $E_{IR,S} = A_{IR,S}$ and is close to the black body value of 1.0. Calibration of mV output with a standard radiant source thus provides only the net energy exchange, but not the down-welling component. If this voltage response is linear, as for our pyrgeometer, a single sensitivity factor S in units of [(mV)/(Wm⁻²)] results, and *net* input of radiant power density is then (mV)/ S Wm⁻². The sensitivity S of our MS-202 thermopile to absorbed radiation was pre-calibrated on January 5, 2012 giving $S = 3.83 \times 10^{-3}$ mV/Wm⁻². To extract down-welling irradiance the output radiance must first be determined, then added to the net input term to extract the desired down-welling component. The actual body temperature of the sensor system, which for the pyrgeometer is labelled T_B (in °K), is thus measured giving output intensity of $E_{IR,S} \sigma T_B^4 = \sigma T_B^4$ with $\sigma = 5.67 \cdot 10^{-8}$ Wm⁻² K⁻⁴ the Stefan–Boltzmann constant. The MS-202 thus yields long-wave down-welling thermal radiation intensity $IR_{DW}(PYG)$ (pyrgeometer)) given by

$$IR_{DW}(PYG) = \left[\frac{(mV)}{S} \right] + \sigma T_B^4 \text{ (W/m}^2\text{)} \quad (1)$$

The use of down-welling infrared measurements from the sky is of particular interest for use with building energy simulation software such as EnergyPlus [15] to calculate temperatures, cooling and heating loads, and the building thermal performance [12,16,17]. We will demonstrate that good data is preferable to approximate sky models for input to simulation models under all sky conditions. Rather than calculating IR_{DW} approximately using weather conditions and cloud coverage, as is often done, this paper presents a methodology to measure and calculate with a simple probe. Results are well within ± 10 W m⁻² of the intensity from the standard pyrgeometer for clear and fully overcast skies, and for around 60% of data points for more general sky conditions. The atmospheric long-wave down-welling radiation probe deployed is the MLX90614, a low-cost infrared thermometer. Our accuracy range can be improved for general sky conditions using one or more

additional probes set to sample different segments of the sky. Even for one suitably oriented probe general data will be shown to yield dynamic thermal simulation for buildings which closely match model results using data from the expensive instrument.

As noted, IRT sensors have also been used for related atmospheric studies [10,11]. The main response difference between the IRT and the MS-202 is that the former's spectral response cuts-off at 14 μ m. This is less of an issue if radiant source temperature is high for normal non-contact sensing, as then the Planck black body spectrum shifts to shorter wavelengths. The atmospheric radiation spectrum can extend to ~ 30 μ m but most of its energy comes from below 15 μ m with a peak intensity near 10 μ m for cloudy skies and 7.5 μ m for clear skies. In addition its spectral radiance beyond 14 μ m is largely fixed near that of the Planck spectrum at these wavelengths. That is this zone is almost insensitive to cloud cover and humidity. It varies slightly with temperature (as does the whole spectrum). Such characteristics mean calibration of the IRT will involve a near constant component beyond 14 μ m, which means variable spectral response will not introduce significant systematic errors. One goal is then to validate this experimentally. To confirm the accuracy of data collected using the MLX90614 IR thermometer, comparative data was also simultaneously captured using the EKO MS-202 Pyradiometer. The cost differential is a factor of order 350, and the small footprint and weight of the IRT sensor means it can be easily deployed at multiple urban sites where some incoming thermal radiation may come from surrounds. Here however we focus on the main parameter of interest, radiation from the full sky hemisphere.

The technique was developed as follows. The temperature of the sky is measured for many different detector orientations via angles to the zenith, and also checked for some axial variations. The average value of the atmospheric long-wave down-welling radiation is then estimated for each segment of the sky vault. Based on the representative angle concept we proceed to establish from experiment the direction the IRT can point to measure mean clear sky radiance. An experimental value of $\theta_R(\Omega)$ was needed, as it may differ from the well known value for very small Ω . That is one cannot assume that $\theta_R(\Omega) \sim \theta_R(0)$. The aim is thus to match the average at the chosen orientation, to the whole sky average given by the pyrgeometer. Thus after sky segment data is processed the thermometer was orientated to the zenith angle which provided the average value of the atmospheric long-wave down-welling radiation of the whole sky.

2.1. The infrared thermometer

The MLX90614 was used. It is an infrared thermometer for non-contact temperature measurements. A long-wave pass optical filter



Fig. 2. MLX90614 infrared thermometer. Source: <http://learn.adafruit.com>.

is integrated into the package. The wavelength pass band of this optical filter is from 5.5 μm to 14 μm and cuts off the visible and near infrared to provide ambient and sunlight immunity [18]. The MLX90614 is shown in Fig. 2.

Fig. 3 shows its use in SMBus (system management bus) configuration. The sensor is connected to the LabJack U3-HV, a device which provides analog and digital inputs/outputs, which are input via a cable with USB connector to a computer and hence easily managed [19].

The Vss line of the MLX90614 unit is directly connected to ground. Two 4.7 k resistors are used as pull up resistors and a decoupling capacitor is installed between VS and ground.

3. Methodology

As explained in the introduction, it was established long ago that a thermal radiation sensor with a small field of view can point in a fixed direction to the zenith, called the “representative angle”, to measure mean clear sky radiance. This follows from the known variation under clear sky conditions of the observed sky radiance $\Phi_{\text{SKY}}(d\Omega)$ in $\text{Wm}^{-2}\text{Sr}^{-1}$, with solid angle $d\Omega = \sin \theta d\theta d\phi$ in radial direction (θ, ϕ) . θ is the angle of tilt to the zenith, and ϕ the axial angle. This variation can be used to theoretically validate the observed value for small Ω , of $\theta_R = 52.5^\circ$ to the zenith. This concept is extended here to allow for a representative angle for a clear sky radiation sensor in which the sensor has a larger but still restricted field of view, as occurs with most low cost infrared thermometers. The same clear sky models indicate that a broader field of view can still lead to a “representative angle”. The tilt for our IRT is determined experimentally in this study.

$\Phi_{\text{SKY}}(d\Omega, \lambda)$, the spectral radiance around (θ, ϕ) varies with humidity. Humidity closes up the sky window from 8 to 13 μm , hence raising incoming radiance. For example the minimum atmospheric radiance near 10 μm is $\sim 1 (\text{Wm}^{-2})\text{Sr}^{-1}(\mu\text{m})^{-1}$ for 1.5 cm of water in the atmospheric column and $\sim 5.5 (\text{Wm}^{-2})\text{Sr}^{-1}(\mu\text{m})^{-1}$ for 6 cm [4,20]. For a clear or uniform sky the transmittance of the atmosphere falls as θ increases [4,20] and rays pass through more atmosphere. Let atmospheric thickness be d along a radial direction from earth's centre, hence at the zenith. If atmospheric absorptance for radiation, which varies with gas content, is α per meter then at $\theta = 0^\circ$ the zenith transmittance $T_A(0) = C\exp(-\alpha d)$ with C found experimentally. For a finite zenith angle θ , $d(\theta)$ becomes $[d/\cos\theta]$ and hence $\ln(T(\theta)) = [1/\cos(\theta)] * [\ln T_A(0)]$. The absorptance $A_A(\theta)$ and emittance $E_A(\theta)$ of the atmosphere thus rises as θ increases from 0° at the vertical. Equation (2) expresses this rise in terms of $T_A(0)$.

$$E_A(\theta) = 1 - [T_A(0)]^{\frac{1}{\cos(\theta)}} \quad (2)$$

This equation leads to the conclusion that under clear skies at a special or representative tilt angle of 52.5° , the reading of a narrow viewing IR sensor whose field of view $\Delta\Omega$ approaches zero will allow a good estimate of the mean down-welling radiation from the whole sky. If $\Delta\Omega$ is much larger (in our IRT half cone angle is near 40°), a representative angle still exists, as found experimentally here. However it is expected to change from that when $\Delta\Omega$ approaches 0° .

The infrared thermometer measures the incoming radiation. It then assumes the emitting hemispherical body is uniform with emissivity of 1.0 to yield its effective temperature T_{SKY} . This will be lower than $T_{A,t}$ the atmospheric temperature, by variable amounts which depend on cloud cover and humidity. The difference between $T_{A,t}$ and T_{SKY} is largest for a clear, dry sky. The “emitting body” in this work is a segment of the sky vault given by the acceptance solid angle $\Delta\Omega$ of the IR sensor, plus its tilt and axial setting. Its field of view about its normal is plotted in Fig. 4. To set the IRT orientation the apparent temperature of each portion of sky is first measured in $^\circ\text{C}$ with the IRT sensor set at many different (θ, ϕ) directions under a clear sky using the pan tilt stage shown in Fig. 5. The sky was divided into different segments, using data at eight zenith angle settings across each of four axial plane used, plus the vertical. The total was thus 33 segments of the sky. The average value of the atmospheric long-wave down-welling radiation is calculated for every area. The effective temperature of the viewed sky segment is the output of the MLX90614 infrared thermometer. It is first converted to its Kelvin value T_{SKY} so that the total atmospheric long-wave down-welling radiation from that sky segment can be found. If the IRT sensor sets an effective uniform atmospheric emittance of 1.0 it is in effect replacing a spectrally non-uniform radiance with a uniform black body at $T = T_{\text{SKY}}$ so as to equate actual radiance with that of the equivalent black body. Down-welling thermal radiation given by the IRT for the whole sky is then

$$\text{IR}_{\text{DW}}(\text{IRT}) = \sigma(T_{\text{SKY}})^4 (\text{W/m}^2) \quad (3)$$

Finally all the effective values of $\text{IR}_{\text{DW}}(\text{IRT})$ per zone are combined to yield the average value of the atmospheric long-wave down-welling radiation of the whole sky. This value is then compared to all effective values per zone and the infrared thermometer is orientated to the angle where the reading matches the total value of radiant intensity. Fig. 5 shows the MLX90614 infrared thermometer located on the roof of the Faculty of Science building

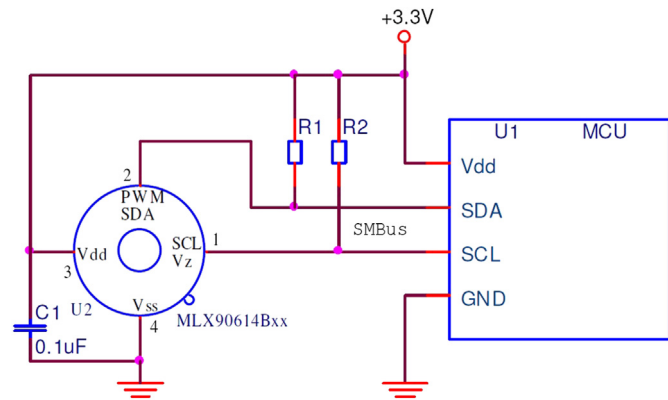


Fig. 3. MLX90614 SMBus connection. Source: Melexis [18].

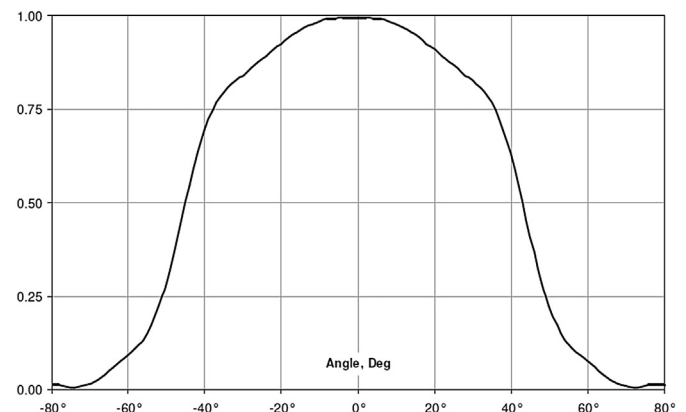


Fig. 4. Relative sensitivity of the IR sensor to radiation as angle of incidence moves away from the peak value at its normal. Source: Melexis [18].

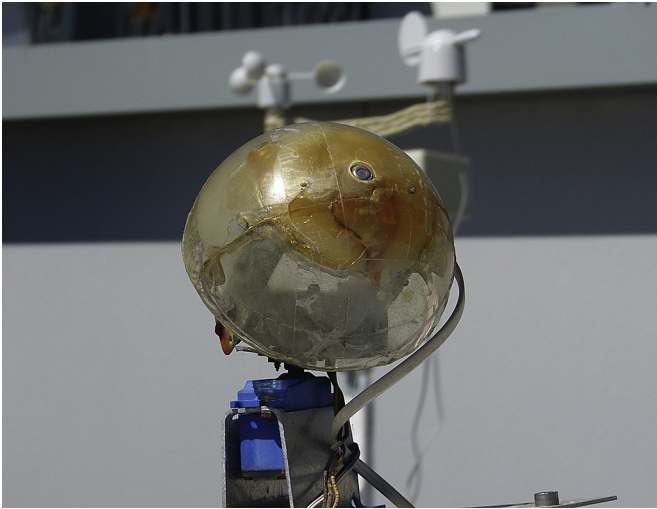


Fig. 5. MLX90614 infrared thermometer mounted on a pan tilt stage located on the roof of the faculty of Science at University of Technology, Sydney.

at UTS (University of Technology, Sydney) [latitude/longitude = 33.9°, 151.2°] and oriented to the appointed angle which was found to be 55° to the zenith. The infrared thermometer was attached to a pan-tilt stage to enable mapping of the incoming sky radiation if desired. From this angular data it was evident by comparing the pyrometer data that measuring the $E_A = 1.0$ effective sky temperature at approximately 55° to the zenith gave in general a good approximation when used in Equation (3) to the $IR_{DW}(PYRG)$ direct reading. We then fixed the angle of the infrared thermometer and did a seasonal comparison with the full sky radiation given by Pyrometer EKO MS-202. This IR data set

complements simultaneous weather station data (temperature, humidity, wind, direct solar, global horizontal solar). Real time EnergyPlus weather data sets could then be produced. The atmospheric long-wave down-welling radiation provided by the infrared thermometer differs from the value gathered by the pyrometer if cloud cover varies a lot with direction. However detailed comparisons following of many thousands of pyrometer and IRT data points indicates most results provided by the infrared thermometer are well within the desired uncertainties for clear skies and homogeneous skies of 10 W m^{-2} . Around 80% of all data points for clear skies also lie within this desired range. The measured value is the average temperature of all objects in the field of view of the sensor. Fig. 4 shows for the small IRT sensor the variation of its relative sensitivity with direction. This plot yields the field of view, hence the solid angle of the sky vault from which radiation is accepted.

4. Evaluating irradiance accuracy given by the tilted IR temperature sensor

Figs. 6 and 7 plot the actual readings at each sampling time of both IRT and pyrometer as well as the difference in each such pair. The two raw data sets were taken every minute over twelve winter and six summer days respectively by the two methods of sensing incoming IR sky radiation. Over 17,000 and 8500 data pairs were thus taken respectively to yield these differences. The highest density of error data points is near zero in the winter period but a slightly high average IRT value by 10 W/m^2 occurs in summer. What is also clear from both these plots is that errors are smaller and in a tight range at night but extend to higher values and cover a wider range in the day. The largest errors occur mostly when daytime values are near their peaks. The plots also show via the ability to discern separate data points easily, that these larger errors occur

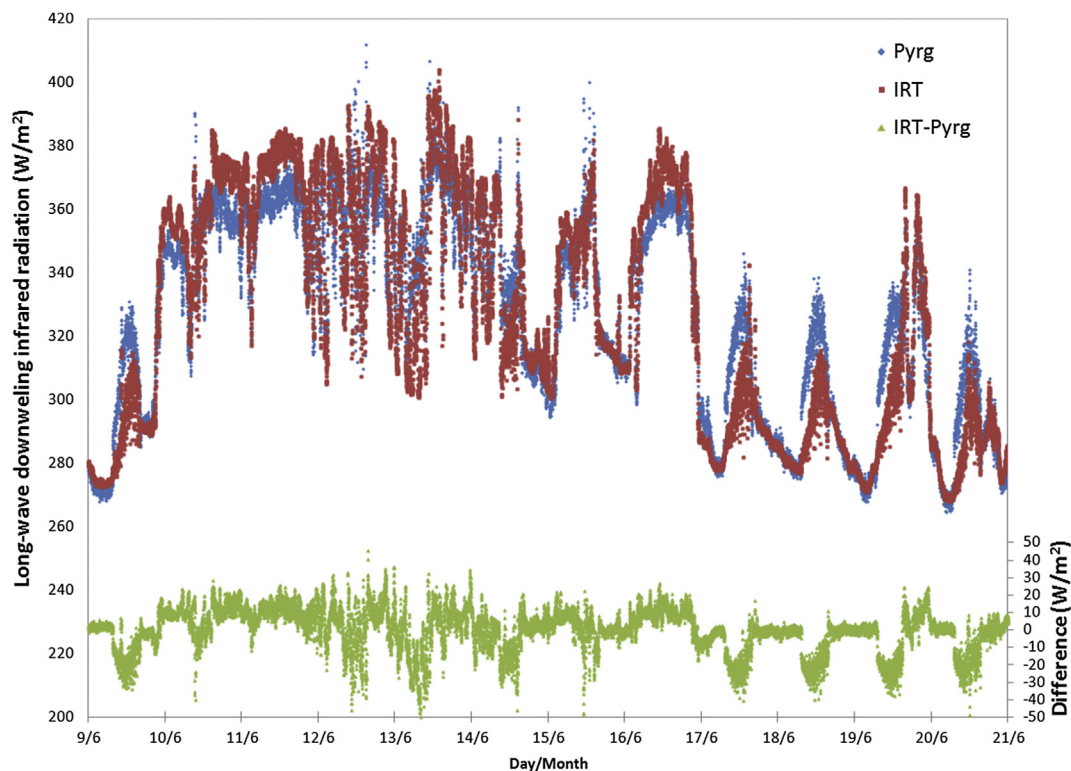


Fig. 6. Atmospheric long-wave down-welling radiation (point-by-point) from IRT and pyrometer readings in winter from the 9th to 21st of June 2012, (left axis) and the error or difference between each pair (right axis). Date marks indicate midnight.

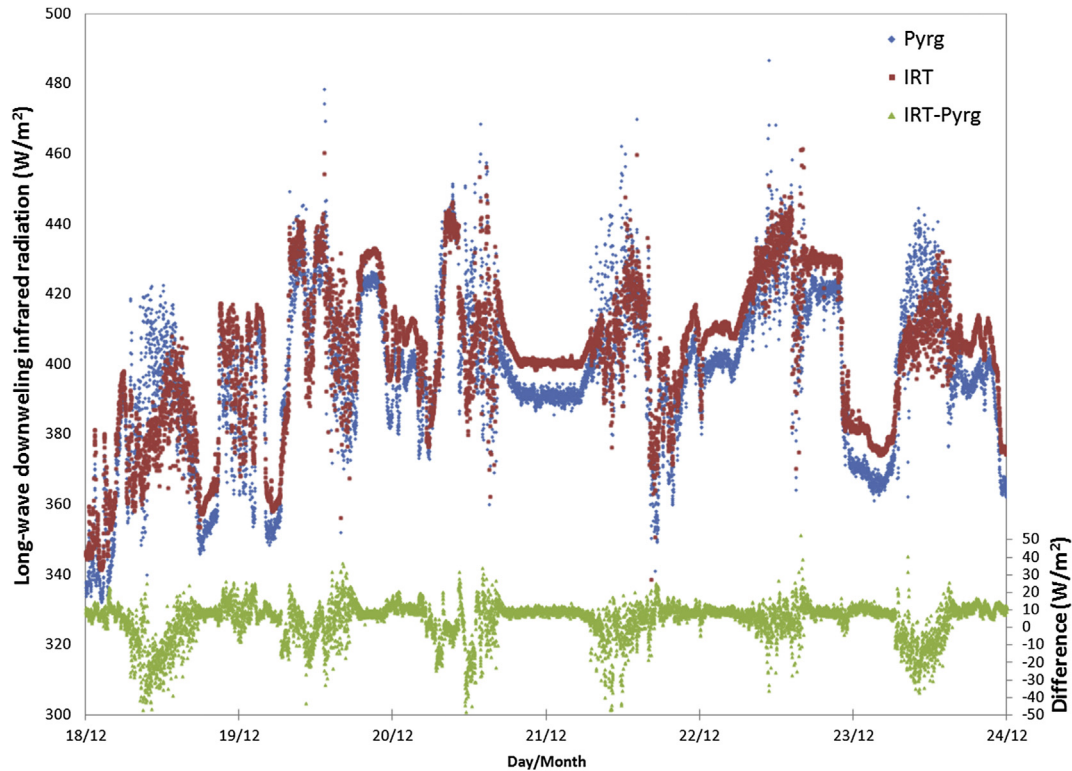


Fig. 7. Atmospheric long-wave down-welling radiation point-by-point (left axis) and differences in each pair (right axis) for the IRT and pyrgeometer. Readings in summer from the 18th to 24th of December 2012. Date marks indicate midnight.

quite infrequently compared to the low error cases. This again links to average differences in cloud patterns overnight relative to the day, which in turn probably links to greater daytime dynamics or calmer weather at night. That large discrepancies arise under some but not all conditions is also obvious. A more rigorous quantitative analysis of differences follows that shows the method is valid within $\pm 10 \text{ W m}^{-2}$ for a significant majority of data points and errors are very small for clear skies. This is despite for a few data points differences in Figs. 6 and 7 extending to beyond 40 W m^{-2} . These will be for highly anisotropic cloud cover, when inhomogeneous skies are most likely. As the tilted IR thermometer measures part of the sky rather than the whole hemisphere when clouds approach from the opposite direction the greatest discrepancies are observed, as expected. This could be corrected for by measuring more segments of the sky. For example using four IR thermometers at the same zenith angle tilt but facing different equally spaced azimuthal directions: such as north, south, east, and west. An average of their output would better represent the whole sky radiance when clouds are distributed anisotropically. This would still be a very low cost system, at about 1/70th of the cost of the pyrgeometer. A simplistic discussion of uncertainty is not appropriate to this IRT data as the relative agreement between the two instruments depends strongly on variations in sky conditions, hence weather, time of day and time of year. Slight differences in timing responses when large shifts occur are apparent in these two figures. These are most obvious in winter and not seen in summer. They may be influenced by sensor field of view as well as cloud distribution. Deeper insights into the link between their deviations and sky conditions indicates in advance when results are going to be accurate to within 10 W m^{-2} but also acts as a measure of degree of in-homogeneity in sky coverage. Thus if four IRT probes were deployed not only would accurate $\text{LW}_{\text{D-W}}(\text{IRT})$ data follow, but comparison among them would quantify relative cloud cover in sky segments and its changes over time.

We now present a number of approaches to analysing uncertainty in the IRT data because of the need to identify various factors that influence it. One can study for example, differences or errors in actual energy flows, which are ultimately of most interest. Variation of average differences and the magnitude of standard deviations as radiance intensities vary are of special interest. They lead to variations in accuracy with season, and with sky conditions. Finally and more basically overall percentage errors across all readings can be studied. They can show whether there are any significant systematic errors due to issues in either the optical sensing ranges, photo-thermal voltage responses, estimates of output radiance, or acceptance angle and sky view differences between each sensor type.

To test the accuracy using the infrared thermometer, the atmospheric long-wave down-welling radiation has been recorded and analysed each minute during the following five periods: 9th of June to 11th of July 2012 (mid-winter); 22nd of August to 6th of September 2012 (early spring); 2nd of November to 15th of November 2012 (late spring); 18th of December to 17th of January 2013 (mid-summer); 19th of March to 4th of May 2013 (autumn). The deviation ranges of all the values taken have been binned into 0.01 intervals in deviation D as given in Equation (4) which uses results from Equations (1) and (3) respectively.

$$D = (\text{IR}_{\text{DW}}(\text{PYG}) - \text{IR}_{\text{DW}}(\text{IRT})) / \text{IR}_{\text{DW}}(\text{PYG}) \quad (4)$$

If the sign of D is positive, it means that the pyrgeometer gave a higher value than the infrared thermometer, if negative the infrared thermometer provided a higher value than the pyrgeometer.

4.1. Measured accuracy from the 9th of June to the 11th of July 2012

As an example of the spread of deviations data in one season (mid-winter) from the 9th of June to 11th of July 2012 is described

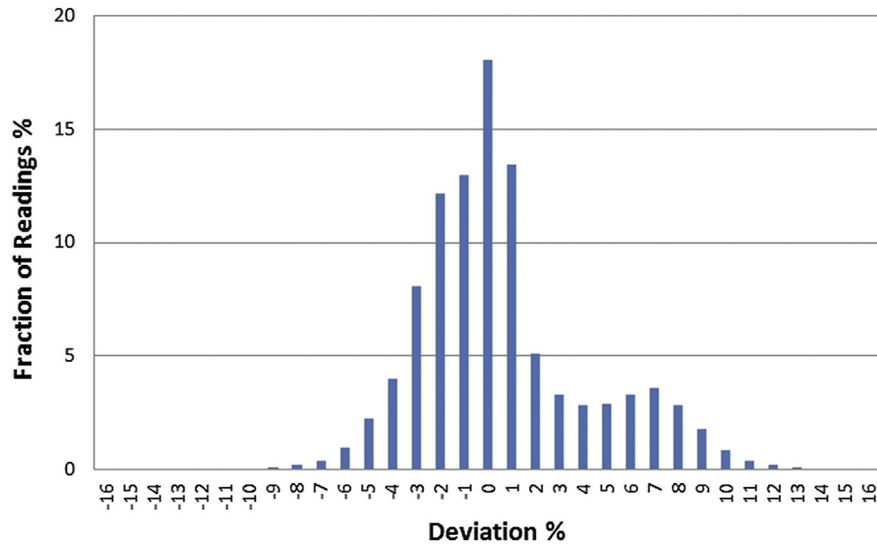


Fig. 8. A representation of the number of times a given data point defined by Equation (4) falls in a set deviation interval (as a % of all readings acquired). Positive deviations mean a low reading with the IRT chip, and negative means it is high. The vertical axis is the percentage of data occurring in each interval. Readings bigger than -1% and smaller and equal than 0% are represented in the x-axis as 0% deviation. Data period June 9 to July 11, 2012.

in this section. Similar analysis for other periods is included later in a summary table. A break up or distribution of percentage differences to the pyrgeometer with the simple IRT approach, including sign, is useful and is illustrated in Fig. 8.

The relative distributions of high and low readings of the IRT thermometer are observed in such plots. Any asymmetry in the plots links to the distribution of cloud cover. When it is more strongly or more weakly distributed on average in the direction to which the IRT sensor points, such differences are expected. In the data in Fig. 8 the secondary peak, which is for low readings on the IRT, and the wider spread of low readings compared with high IRT values, indicates that the sky is more often in-homogeneous in one direction. Fig. 10 following for the same period shows such points occur with relatively low frequency. This is when clouds are more likely to be found in the sky portion behind the sensor direction. This direction is in fact where more cloud cover builds up in Sydney as frontal systems approach. We also found larger divergences occurred more in warmer summer days when storm fronts often arise, and they come typically from the south-west. The sensor however was tilted in a plane bearing north-west. Table 1A and 1B

also show overall that most results from the sensor have excellent accuracy for simulation for more homogeneous skies, which yield the lowest and highest incoming radiation and are more common on average.

The bar chart in Fig. 9 is an alternate representation of accuracy showing the accumulated fraction of IR sensor readings that lie within a given % of those from the pyrgeometer. For example 93% lie within 7% of the correct reading and 76% within 4%. Given the asymmetry seen in Fig. 8 averages remain close to the sensor reading.

Fig. 10 provides additional insights via the correlation of accuracy to actual atmospheric radiation intensities. The values of the atmospheric long-wave down-welling radiation obtained by the infrared thermometer are plotted against those from the pyrgeometer. The straight line shown is the reference line for equality. The density of data pairs at any point on the graph is also shown via colour and is in effect a visual indication of the frequency of pairings, and via separation from the equality line the frequency of different accuracy levels. What is interesting about the accuracy as shown in the manner of Fig. 10 is that it varies systematically with

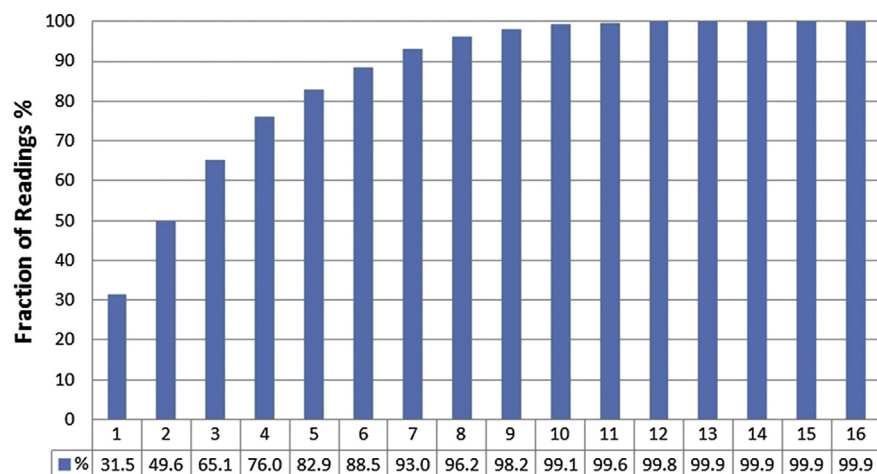


Fig. 9. Accumulated percentage of IR sensor readings every minute from the 9th of June to 11th of July 2012, which lie within a given maximum error range.

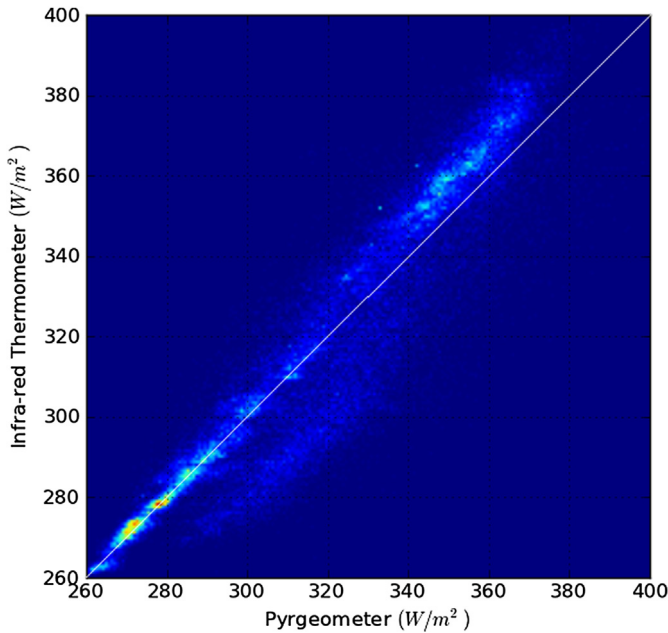


Fig. 10. Inter-comparison plot of atmospheric long-wave down-welling radiation measured by the IR thermometer and the pyrgeometer for many thousands of single data pairs, over the winter period of 9th of June to 11th of July 2012. The solid line represents the plot for no error. Points above mean IRT values are high, while below they are low.

the intensity of incoming radiation. Lowest spread in values and very high accuracy are at intensities below 300 W m^{-2} when skies are mostly clear and drier. These lowest intensities tend to occur at night and specific day night comparisons are given in the next section. The other high-density zone of plot points is from 340 to 365 W m^{-2} in which the thermometer value is consistently high by amounts of $5\text{--}10 \text{ W m}^{-2}$ (in error terms about 2%). These occur in the daytime. These apparent larger radiation errors occur when solar intensity is present and are thus dwarfed by the sum of solar and atmospheric radiant intensity. That is their impact on the accuracy of roof and building simulation predictions are expected to

be almost negligible. Thus day and night the fixed thermometer values should be acceptable for use in simulation studies. In Fig. 10 are other low frequency bands of points with an interesting band of such points in which the thermometer value is least accurate and low by up to 20 W m^{-2} . It is isolated from the equality line and the high frequency, accurate band ranging from 290 to 330 W m^{-2} . This unusual band arises as winter clouds build up in the opposite direction to the IRT sensor's orientation when cold fronts approach from the south-west.

The other four period plots like those in Fig. 10, though shifted to higher intensities in warmer seasons, are qualitatively similar. The largest errors again occur with lowest frequencies and good accuracy arises more frequently at lower intensities. Errors are largest but occur with low frequency when skies are partly cloudy, and also clear in a large sky segment and cloudy in the opposite segment, as when a front approaches. Many intermediate intensity points are also accurate and hence clustered near the equality line. When skies are partly cloudy but approximately homogeneous good accuracy along with partially elevated intensities is expected. To further differentiate the various sources and sizes of errors, an overview of IRT accuracy in terms of average differences from PYG data across five seasonal periods spanning a year follows in Table 1A. Table 1B accumulates all such data over a year into narrow bands of intensity.

Table 1A and 1B were prepared using all data in each period (from 20,000 to 60,000 PYG, IRT total data pairs per seasonal period). Data was then further broken up into a range of $\pm 5 \text{ W m}^{-2}$ about a fixed intensity value. The number of data pairs in each such segment in Table 1a were on average 2,500, predominantly over 350, and ranged up to 6000 pairs. Average differences include the sign of each divergence representing an average bias offset. This is the mean bias error (MBE*) here expressed in intensity terms (rather than as percentage error), and is listed in Table 1A and 1B to indicate whether IRT intensity data is on average high or low. It is accompanied in both tables by the standard deviation from equality for all IRT data in the $\pm 5 \text{ W m}^{-2}$ bands about values listed in the left column. In Table 1A some intensities are only represented strongly in summer or winter. In summer low intensities near $275 \text{ (W m}^{-2})$ rarely occurred, while in mid-winter intensities at 425 W m^{-2} never occurred. Large weather fluctuations occur in Sydney in Spring

Table 1

A. The mean bias error between IRT and PYG radiant intensity readings as a function of the value of intensity from the pyrgeometer, for five extended periods spanning most seasonal conditions. The standard deviation at each intensity band is shown in brackets. A plus sign denotes that the IRT reading is on average high and a minus sign that it is low. **B.** The MAE (mean absolute error) and MBE* (mean bias error) and standard deviation of the difference between IRT and PYG radiant intensity readings as a function of the value of intensity from the pyrgeometer combined over all periods.

| A. | | | | | |
|--|---|--|---|--|---|
| Pyrgeometer reading (W m^{-2}) | Mid-winter Average IRT error W m^{-2} 9th June – 11th July | Early spring Average IRT error W m^{-2} 22nd August – 6th Sept. | Late spring Average IRT error W m^{-2} 2nd – 15th November | Mid-summer Average IRT error W m^{-2} 18th Dec. – 17th Jan. | Autumn Average IRT error W m^{-2} 19th March – 4th May |
| 275 | 0.9 (2.5) | –1.8 (2.2) | N/A | N/A | N/A |
| 325 | –4.6 (14.6) | –12.8 (14.6) | 4.1 (6.3) | 6.0 (3.6) | 7.0 (7.6) |
| 375 | 2.4 (13.2) | –10.8 (16.9) | 3.9 (12.2) | 5.3 (10.9) | 6.8 (12.1) |
| 425 | N/A | N/A | –16.0 (14.3) | –5.0 (14.2) | –1.1 (13.0) |
| B. | | | | | |
| Pyrgeometer reading (W m^{-2}) | MAE IRT deviation (W m^{-2}) | | MBE*IRT deviation (W m^{-2}) | | Standard deviation (W m^{-2}) |
| 250 | 2.6 | | –2.6 | | 1.2 |
| 275 | 2.0 | | 0.1 | | 2.7 |
| 300 | 7.0 | | –2.0 | | 9.6 |
| 325 | 11.2 | | –0.6 | | 13.9 |
| 350 | 10.6 | | 3.1 | | 12.8 |
| 375 | 10.8 | | 5.1 | | 12.3 |
| 400 | 10.3 | | 1.8 | | 13.1 |
| 425 | 11.6 | | –4.8 | | 14.3 |
| 450 | 15.8 | | –12.8 | | 16.0 |

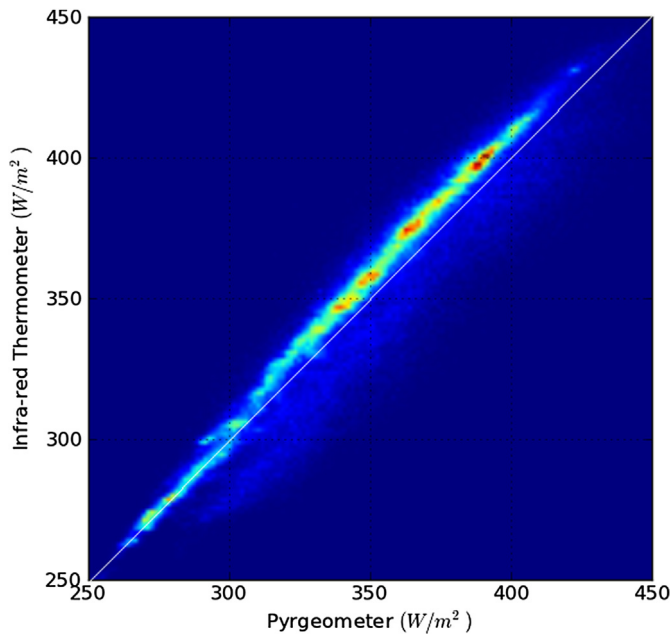


Fig. 11. Inter-comparison plot of atmospheric long-wave down-welling radiation measured by the IR thermometer and the pyrgometer for many thousands of single data pairs, of all 5 periods. The solid line represents the plot for no error. Points above mean IRT values are high, while below they are low.

involving very high winds and cloud movement. That is rapid switching from clear to cloudy skies also occurs.

In Table 1B combining seasonal data means sufficient points are available to use smaller spacing between the intensity bands (still spanning $\pm 5 \text{ W/m}^2$ about each value in the left column (160–2000) for useful statistical error analysis. The upper and lower intensity bands in 1B lie outside those in 1A. They had the lowest pairs of points and were extended to centre on 450 W/m^2 and 250 W/m^2 respectively. Table 1B includes again MBE* and standard deviation for each band, but in addition includes MAE (mean absolute error). MAE most clearly summarises how the likelihood of errors rises as intensity rises. This is also apparent visually in Fig. 11 which includes as in Fig. 10 via colour an indication of the frequency with which particular data pairs and associated errors occur. Table 1B and Fig. 11 indicate three distinct intensity zones in terms of MAE values (a) below 300 W/m^2 MAE values are very low and percentage errors under 1% (b) from 325 to 400 W/m^2 MAE is confined to a narrow range of 10.3 – 11.2 W/m^2 (c) intensities above 400 W/m^2 MAE is largest. Fig. 11 also indicates atmospheric radiant intensities in range (c) occur relatively rarely. These arise in summer daytimes and are mostly associated with storm conditions which typically build up for Sydney in the south-west while our single tilted sensor was pointed towards the north-west.

The smaller average differences and low errors for clear sky, low intensity conditions contrast with the larger errors in IRT data associated with higher intensities. The latter can then be attributed almost entirely to the impact of in-homogeneous skies when cloud cover builds up in one segment of the sky. A single sensor tilted in a fixed vertical plane will then either overestimate or underestimate IR intensity depending where cloud density is highest. A low cost solution to this problem has already been noted. It is also apparent from clear sky and night-time data that systematic errors, for example due to the spectral sensitivity of the IRT relative to the pyrgometer, are not of concern. As noted above when considering the range of errors observed and their dominant timing relative to the total incident solar and/or atmospheric radiation impinging on

a surface day or night we conclude that the use of IRT down-welling data in building simulation is expected to yield quite satisfactory results. An example follows.

4.2. Results comparison between daytime and night time

The 9th June 2012 to 11th July 2012 data on both sensors in winter was separated into two segments, day and night, to assess the influence of solar radiation and daytime temperatures on the accuracy of IR sensor observations and possibly on cloud asymmetry. A comparative analysis for the day and night in summer from the 18th December 2012 to 17th January 2013 was also made. Accuracy analysis using Equation (4) showed that 78% of the IRT values have a deviation of 3% or smaller during the night, in comparison with only 65% during the whole day–night period. 99% of the values measured by IR thermometer differ by less than 7% to those from the pyrgometer during the night compared with 93% during the whole day–night period. Over the whole day–night period average percentage deviation is 2.7%, consisting of 1.9% during the night, and 4.4% during the day.

The comparison between the atmospheric long-wave down-welling radiation measured by the pyrgometer and by the fixed tilt infrared thermometer in one period in winter and another in summer show that instantaneous pair results are generally closer during the night than during the day in both periods.

5. Simulations

To quantify the contribution of various building design parameters [21,22], measurements were gathered in two outdoor matching small structures, each with a single interior zone, and sloping roof of 22° to the horizontal. Each is oriented with its axis aligned east-west. Built with 9 mm wood, the two outdoor matching structures have 120 mm rigid polystyrene insulation (R-value 2.8) on the floor and 60 mm rigid polystyrene insulation (R-value 1.4) under the roof and against the walls, the footprint of the small scale building is $2 \text{ m} \times 2 \text{ m}$. The height in the lower side is 1.4 m, and the maximum or apex height is 1.6 m. These matching structures are located on the roof of the Faculty of Science building at University of Technology Sydney (UTS). Weather files for EnergyPlus were created to perform the simulations, with data from (i) a weather data station which gave temperature, humidity, dew point, wind direction and velocity, air pressure, and rainfall (ii) a pyranometer which gave solar irradiance (direct normal, diffuse, global horizontal) (iii) the MS-202 pyrgometer and the tilted MLX90614 infrared thermometer which both supplied atmospheric long-wave down-welling radiation after processing. Two sets of simulation were performed from the 13th to the 15th of April 2013, using down-welling radiation from the pyrgometer and from the infrared thermometer to model their impact on roof and room temperatures. EnergyPlus (energy building analysis and thermal load simulation program) software is used to model the temperatures. The TARP DOE-2 model was chosen to perform the simulation, which uses the classes SurfaceConvectionAlgorithm:Inside = TARP and the SurfaceConvectionAlgorithm:Outside = DOE-2. Fig. 12 shows a comparison between modelled values of roof and room temperatures for the matching small structures using the long-wave down-welling radiation gathered by the pyrgometer and infrared thermometer. The percentage deviation during this period is 2.7%, 2.6% during the night and 2.9% during the day.

Although the percentage deviation is small, we can see differences during the night mainly for the roof. The error is largest when the sky is clear and the roof is coldest. A smaller error ($<1^\circ \text{C}$) occurs in the room temperatures when the roof discrepancy is largest.

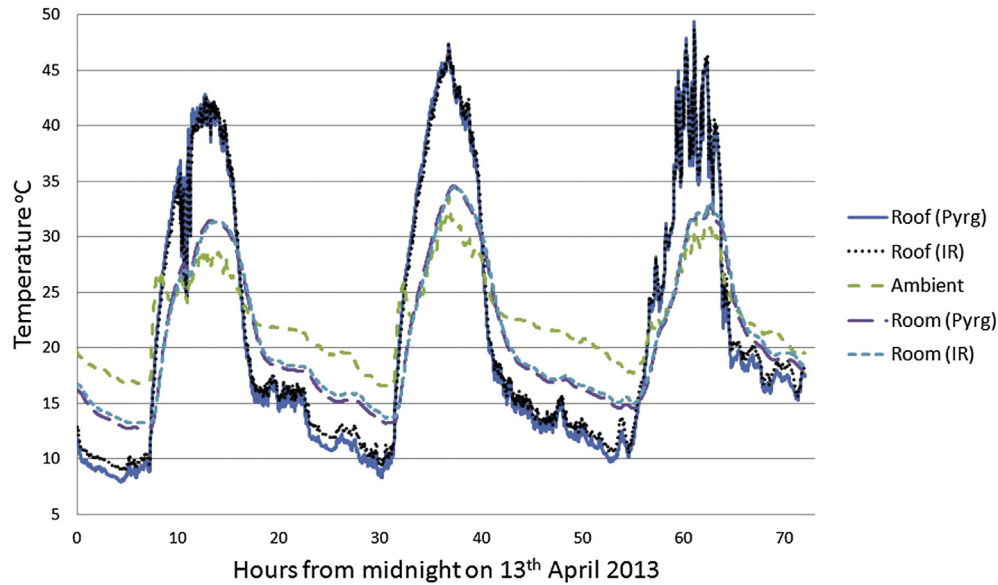


Fig. 12. Comparison between modelled values of roof and room temperatures at the matching small structures using the long-wave down-welling radiation gathered by the pyrgeometer ("Pyrg") and infrared thermometer ("IR").

During the night in this period the infrared thermometer provided higher long-wave down-welling radiation than the pyrgeometer which means more incoming atmospheric radiation from the sky to the building if used in models. T_{SKY} will also be higher so less outgoing radiation from the roof to the sky, leading to higher roof and room temperatures at the outdoor matching small structures. The average percentage deviation between sensors is higher during the day than during the night, however this has little impact on simulation as long-wave down-welling radiation affects building temperatures much more during the night than during the day. This is because solar radiation dominates incoming radiance during

the day and roofs then are hotter so outgoing thermal radiation is also much larger. Infrared radiation values gathered by the pyrgeometer and infrared thermometer are shown in Fig. 13 which compares them to sky models. Both measurements follow similar temporal patterns especially during the night. These results show the importance of accurately considering long-wave down-welling radiation in building thermal performance and building energy efficiency studies at night.

When down-welling radiation is not measured it is often calculated using the following weather data: dew point temperature (T_{DEW}), dry bulb temperature (T_{DB}), both in K, and opaque sky

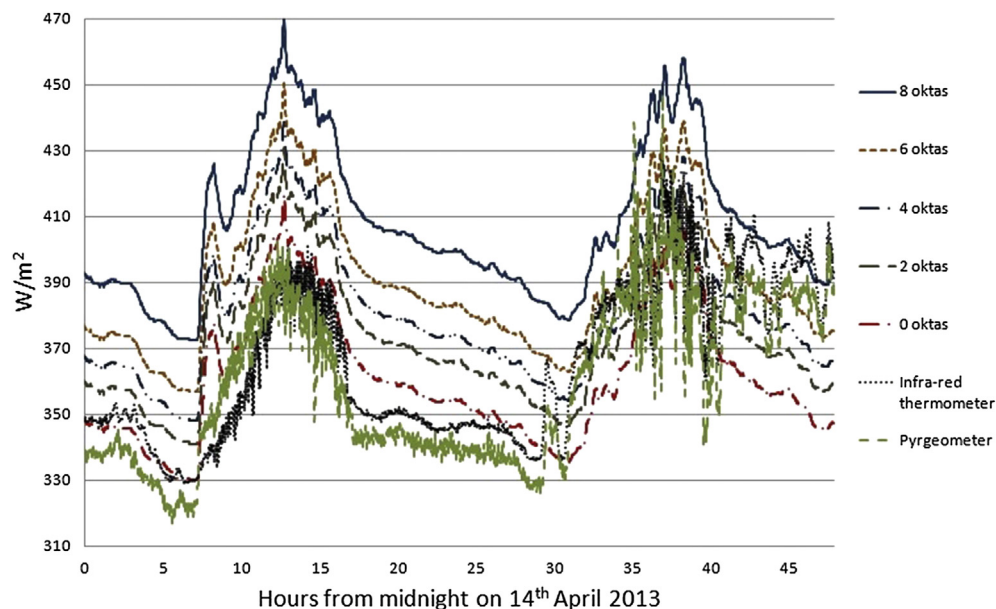


Fig. 13. Atmospheric long-wave down-welling radiation comparison between calculations from 0 to 8 oktas, and infrared thermometer and pyrgeometer measurements on two days starting from midnight 14th of April 2013. The first day and the whole night have almost clear skies. The second day has variable cloud cover.

cover O_{SKY} measured in oktas [23]. To calculate IR_{DW} , whole sky effective emissivity E_{SKY} must first be calculated. E_{SKY} and IR_{DW} are estimated using Equations (5) and (6) respectively:

$$E_{SKY} = [0.787 + 0.764 \log (T_{DEW}/273)] \times [1 + 0.0224O_{SKY} - 0.0035O_{SKY}^2 + 0.00028O_{SKY}^3] \quad (5)$$

$$IR_{DW} = E_{SKY} (\sigma T_{DB}^4) \quad (6)$$

Atmospheric long-wave down-welling radiation has been calculated from 0 to 8 oktas from the 13th to the 15th of April 2013. Oktas, representing the area of sky cloud coverage in eighths, are normally estimated by people looking at the sky, but only during the day. Uncertainty on the oktas present is one reason why it is important to measure down-welling infrared radiation. Fig. 13 shows that even if cloud coverage is known, and even in times of clear sky (0 oktas) which works best, the approximate equations often over-estimate the atmospheric long-wave down-welling radiation. Hence cooling rates based on this approach are often under-estimated.

6. Conclusions

The accuracy for a single low cost, small IRT (infrared thermometer) as a fixed sensor for atmospheric radiation using a PYG (pyrgeometer) as reference, had several interesting features. A representative tilt angle for clear skies was established. Its use in a fixed vertical plane was the main source of errors, when they arose outside the goal of less than 10 W/m^2 . Errors were thus examined in various ways. Overall distributions and their deviations for several thousand data points were analysed. These were repeated for a range of $\pm 5 \text{ W/m}^2$ about particular sky radiation intensities to establish sensitivity to weather linked sky conditions. These analyses then indicated that IRT sensor characteristics were not a significant source of errors. The inability of the fixed mounting system to provide accurate full sky intensities for all cloud cover situations was, as anticipated, the main problem. Accuracy was generally acceptable if not always within desired limits. It was found to be sensitive to season, to time of day, and to the actual intensity of incoming radiation. Systematic errors were very small, and capped at 3 W/m^2 at lower or clear sky intensities. The associated spread of differences was also small for these conditions. Such intensity conditions and lower spread were also found to occur more often at night in Sydney, than in the day. Divergences outside 10 W/m^2 occurred for a moderate to small minority of readings and in the day-time. The sub-division of error analysis into five periods, and for each of these into narrow intensity ranges, each showed distinct sensitivities, which were also linked to the extent of average inhomogeneity in cloud cover.

Thus this light weight, portable and compact sensor is well suited to short term studies in remote and urban areas, though four such IRT sensors would enhance accuracy, and provide more detailed relative cloud cover information, still at low cost. We have utilised this technique using the infrared thermometer at other sites to enable full weather data sets, including down-welling infrared to be measured to create weather files used by energy building simulation software [17]. Since IRT accuracy is lowest when solar intensity is present and thermally dominant, the overall impact on simulation accuracy is small even if using a single IRT sensor. It may also prove useful in studying thermal radiation flows in various urban high rise environments which are of interest to UHI studies, especially at night. Cool roofing is

central to both UHI mitigation and energy efficient building studies [2,4,24,25]. Net radiative flows from roofs and within urban canyons at night are a core aspect of roof, and urban cooling. Building interiors will also cool if overall thermal design is optimized to include those surfaces which enable roofing and façades to cool below ambient at night, and to not get excessively hot during the day.

Acknowledgements

Jose L. Castro Aguilar acknowledges support for his PhD studies from UTS Doctoral Scholarship (UTSD) from the University of Technology, Sydney and the CSIRO Energy Transformed Flagship scholarship.

References

- [1] Sakai S, Ito A, Umetani K, Iizawa I, Onishi M. A practical pyrgeometer using a representative angle. *Am Meteorological Soc* 2009;26:647–55.
- [2] Carter G. Issues and solutions to more realistically simulate conventional and cool roofs. In: *Proceedings of Building Simulation 2011: 12th Conference of international building performance simulation association (IBPSA)*. Sydney, 14–16 November 2011; 2011.
- [3] Akbari H, Menon S, Rosenfeld A. Global cooling: increasing world-wide urban albedos to offset CO_2 . *Clim Change* 2009;94:275–86.
- [4] Smith GB, Granqvist CG. *Green nanotechnology solutions for sustainability and energy in the built environment*. Taylor and Francis. Boca Raton, FL USA: CRC Press; 2010.
- [5] Philipona R, Dutton EG, Stoffel T, Michalsky J, Reda I, Stifter A, et al. Atmospheric longwave irradiance uncertainty: pyrgeometers compared to an absolute sky-scanning radiometer, atmospheric emitted radiance interferometer, and radiative transfer model calculations. *J Geophysical Res* 2001;106(D22):129–41.
- [6] Dines WH. The ether differential radiometer. *Quart. J R Meteorological Soc* 1920;46:399–406.
- [7] Dines WH, Dines LHG. Monthly mean values of radiation from various parts of the sky at Benson. *Mem R Meteorol Soc* 1927;2:1–8.
- [8] Robinson GD. Notes on the measurement and estimation of atmospheric radiation. *Quart. J R Meteorological Soc* 1947;73:127–50.
- [9] Dalrymple GJ, Unsworth MH. Long-wave radiation at the ground: III A radiometer for the 'representative angle'. *Quart. J R Meteorological Soc* 1978;104:357–62.
- [10] Mims III FM, Chambers LH, Brooks DDR. Measuring total column water vapor by pointing an infrared thermometer at the sky. *Bull Am Meteorol Soc* 2011;92:1311–20.
- [11] Morris VR, Long CN, Nelson D. Deployment of an infrared thermometer Network at the atmospheric radiation measurement program Southern Great Plains climate research Facility. In: *Sixteenth ARM science Team Meeting Proceedings*, Albuquerque, NM, March 27–31, 2006; 2006.
- [12] Smith GB, Aguilar JLC, Gentle AR, Chen D. Multi-parameter sensitivity analysis: a design methodology applied to energy efficiency in temperate climate houses. *Energy Build* 2012;55:668–73.
- [13] Aguilar JLC, Smith GB, Gentle AR, Chen D. Optimum integration of albedo, sub-roof R-value, and phase change material for cool roofs. In: *Proceedings of Building Simulation 2013: 13th Conference of the International Building Performance Simulation Association*. Chambéry (France), 25–28 August 2013; 2013.
- [14] Eko Instruments Co, Ltd. *Pyrgeometer MS-202 instruction manual*. December 2011.
- [15] EnergyPlus. <http://apps1.eere.energy.gov/buildings/energyplus/>. U.S. Department of Energy – Energy efficiency and Renewable Energy.
- [16] Gentle AR, Aguilar JLC, Smith GB. Optimized cool roofs: integrating albedo and thermal emittance with R-value. *Sol Energy Mater Sol Cells* 2011;95:3207–15.
- [17] Aguilar JLC. *Building thermal performance and the urban heat island: optimization in temperate zones* [PhD thesis]. Sydney: University of Technology; 2014.
- [18] Melexis. MLX90614 Family single and Dual zone Infra Red thermometer in TO-39, 2013.
- [19] Labjack. Melexis MLX90614 IR Temperature Sensor – I2C. 2013. <http://labjack.com/support/app-notes/mlx90614-ir-temperature-sensor-i2c>.
- [20] Smith GB. Amplified radiative cooling via optimised combinations of aperture geometry and spectral emittance profiles of surfaces and the atmosphere. *Sol Energy Mater Sol Cells* 2009;93:1696–701.
- [21] Bambrook S, Sproul A, Jacob D. Design optimisation for a low energy home in Sydney. *Energy Build* 2011;2011(43):1702–11.
- [22] Cappelletti F, Gasparella A, Pernigotto G, Romagnoni P. Dynamic analysis of energy performance of different roof systems during the cooling season. In: *Proceedings of building simulation 2011: 12th conference of international*

- building performance simulation association, Sydney, 14–16 November. 2011; 2011. p. 2032–9.
- [23] Berkeley lab. Building energy simulation user news, vol. 28; 8-May 2007.
- [24] Aguilar JLC, Smith GB, Gentle AR, Chen D. Making cool roofs compatible with low heating and cooling loads. In: *Fuelling the Future: Advances in Science and Technologies for Energy Generation, Transmission and Storage*. A. Mendez-Vilas. BrownWalker Press; 2012. p. 530–4. ISBN-13: 978-1-61233-558-2.
- [25] Zinzi M, Agnoli S. Cool and green roofs. An energy and comfort comparison between passive cooling and mitigation urban heat island techniques for residential buildings in the Mediterranean region. *Energy Buildings* 2011. <http://dx.doi.org/10.1016/j.enbuild.2011.09.024>.